Influencing factors in the laser-induced damage threshold of Ta$_2$O$_5$ films prepared with different methods

C. XU[a], D. LIN[a], P. FENG[a], D. LI[b], H. FAN[a], J. QI[a], J. NIU[a], Y. QIANG[a]
[a] *School of Materials Science and Engineering, China University of Mining and Technology, Xuzhou 221116, China*
[b]*Shanghai Institute of Optics and Fine Mechanics, Chinese Academy of Sciences, Shanghai 201800, China*

Ta$_2$O$_5$ films were prepared by electron beam evaporation (EBE), ion-beam sputtering (IBS) and sol-gel methods, respectively. It showed that both the refractive indices and the surface roughness of the films were very relevant to the preparation methods. The laser-induced damaged threshold (LIDT) at 1064 nm and 12 ns of the EBE, IBS and sol-gel films was 8.3, 14.4 and 19.6 J/cm^2, respectively. Although the damage of all the films was initiated from defects, the EBE and IBS films presented the thermal melt damage feature, whereas the sol-gel film showed the damage feature of interaction between thermal melt and stress. The impurity defects and structural defects were the main influencing factors in the LIDT of the EBE and IBS films. For the sol-gel film, not only the defect but also the special structure affected the laser damage resistance. The highest LIDT achieved by the sol-gel film was attributed to the least defects and the network structure.

1. Introduction

Due to the urgent need to develop high power and super energy lasers, it is crucial to improve the laser-induced damaged threshold (LIDT) of optical films because of their vulnerability. As for the nanosecond laser-induced damage, the threshold of high refractive materials determines the ultimate damage threshold of the multilayer films because the former are much easier to be damaged [1-2]. Amongst several traditional high refractive materials such as TiO$_2$, Ta$_2$O$_5$, ZrO$_2$ and HfO$_2$, the refractive index of Ta$_2$O$_5$ is only inferior to TiO$_2$, whereas its LIDT, instead, is higher than the latter. Therefore, Ta$_2$O$_5$ is a hot topic from the beginning of laser damage studies.

Although there are kinds of preparation methods for Ta$_2$O$_5$ film, the methods for preparing it with high LIDT is in scarcity. Electron beam evaporation (EBE) is the frequently used and cost-effective method in Ta$_2$O$_5$ film preparation. With the help of this approach, recent studies focus on the effect of the parameters including substrate temperature, deposition rate, annealing temperature and laser parameter on the LIDT of Ta$_2$O$_5$ film [3-5]. As a result of the high cost of ion-beam sputtering (IBS), the studies on high threshold Ta$_2$O$_5$ film with this approach are comparatively few, but in terms of the optical property and damage threshold, this approach is superior to that of EBE [6-7]. Apart from the above two physical vapor deposition (PVD) methods, a chemical method, sol-gel is also popular in high LIDT film preparation such as ZrO$_2$ and HfO$_2$ except Ta$_2$O$_5$. Rather than using the common precursor

tantalum alkoxides in sol-gel method, TaCl$_5$ is used in our previous studies to make the massive preparation of Ta$_2$O$_5$ films with high LIDT possible [8-9]. The above studies indicate that it is likely to produce high LIDT Ta$_2$O$_5$ films with different preparation methods, which raises an interesting question for us to better understand laser-induced damage: are there any differences among these films properties especially in the perspective of the LIDT? Also, are the influencing factors in the LIDT of the films different? Unfortunately, few comparative researches have been conducted with various methods for preparing Ta$_2$O$_5$ films with high laser damage resistance.

In this paper, the technology optimization of EBE, IBS and sol-gel methods was developed respectively for Ta$_2$O$_5$ film preparation and the film properties (e.g. optics and microstructure) were investigated afterwards. Moreover, the comparative studies on the LIDT of the films prepared by different methods were done with the same testing equipment under the equivalent standard and circumstance. Furthermore, the influencing factors in the LIDT of these films were discussed in detail.

2. Experimental

EBE Ta$_2$O$_5$ films were deposited by using Ta$_2$O$_5$ crushed aggregates as starting material with the purity of 99.99%. The chamber was pumped to a base pressure of 2×10^{-3} Pa and oxygen was introduced to keep oxygen partial pressure of 2×10^{-2} Pa. The baked temperature was

held at 573 K during film deposition. To improve the stoichiometry of the films, annealing at 673 K was performed in air. IBS Ta_2O_5 films were deposited by an ion beam sputtering system with the target of tantalum (99.99%). The sputtering chamber was pumped to a base pressure of 4.0×10^{-5} Pa by cryogenic pump and the baked temperature was 409 K. Ar and O_2 were introduced to RF ion beam sources and target surfaces in the deposition process, respectively. Sol-gel Ta_2O_5 films were prepared according to the previous method with some modifications [8]. In typical synthesis, five gram $TaCl_5$ (99.99%) was added to 90 mL EtOH, then 2.1 mL acetylacetone and 2.5 mL concentrated nitric acid were added while stirring. After 10 min, 4 mL H_2O_2 (30 wt. % in water) was added dropwise with violent stirring for 1 h. The solution was sealed in a glass container and aged at 276 K for a minimum of 6 days. The dip-coated process was performed at 20 mm/min and the coated film was baked at 373 K in the air. All the substrates were BK7 and were cleaned carefully before film deposition.

Transmittance curves were measured using a Lambda 900 spectrophotometer and the wavelength accuracy of the instrument during spectra recording was within 0.08%. The refractive indices and thickness were calculated by Essential Macleod (a thin film design software). The microstructures were determined by a D8 Advance X-ray diffractometer (XRD). The surface topographies were observed with a Dimension V atomic force microscopy (AFM) under ambient conditions. The root mean square (RMS) roughness was calculated from the AFM images. The chemical composition was analysed by X-ray photoelectron spectroscopy (XPS) using focused monochromatic Al-Kα ($h\nu$=1486.6 eV) radiation. The absorption was measured using the surface thermal lensing (STL) method and the sensitivity of the measurement was 1 ppm [10]. The impurity contents were detected by a VG 9000 glow discharge mass spectrometer (GDMS). The LIDT testing was performed in the 1-on-1 regime with ISO standard 11254-1, using a Nd:YAG laser in single longitudinal mode with the repetition rate up to 5 Hz [11-12]. This Q-switched laser produced a TEM_{00} mode with a 12 ns pulse length. The laser was used to provide a far-field circular Gaussian beam (spatially and temporally) at 1064 nm wavelength. The spot size of the beam incident on the sample was 300 μm diameters at $1/e^2$ of the maximum intensity. Ten sites of the sample were exposed at the same fluence and the damaged fraction of the sites was recorded. This procedure was repeated for other fluences until the range of fluence was sufficiently broad to include points of zero damage probability and points of 100% damage probability to develop a plot of damage probability versus fluence. A minimum of ten different fluences were adopted in the test, which contained 100 sites. The LIDT, defined as the incident pulse energy density (in J/cm^2) when the damage occurred at 0% damage possibility, could be obtained by linear extrapolation of the damage possibility data to zero damage possibility. The damage morphologies after laser

radiation were evaluated by a Sirion 200 field emission scanning electron microscope (FESEM).

3. Results and Discussion

Fig. 1 is the transmittance curves and refractive indices of the films. Fig. 1(a) shows that all the films have good optical transmittance. Fig. 1(b) shows that the IBS film has the highest refractive index, and then is the EBE film and the last is sol-gel film. Since the energy of IBS atoms is about two orders of magnitude higher than that of EBE atoms, the IBS film has denser structure than the later. The low deposition temperature makes the sol-gel atoms have the lowest energy and mobility, resulting in the loosest structure and the lowest refractive index. It indicates that the refractive indices of the films are very relevant to the preparation methods.
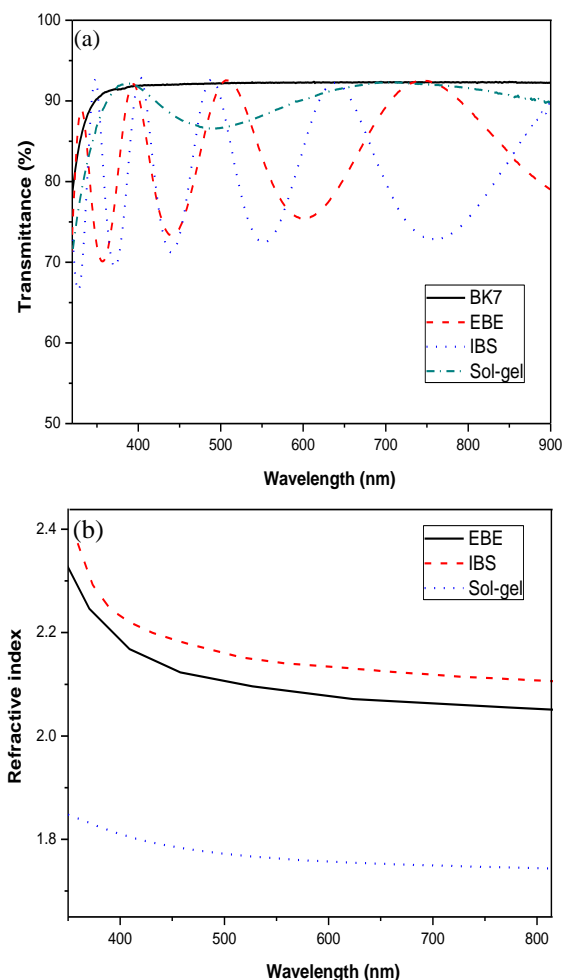
Fig. 1. Transmittance curves (a) and refractive indices

(b) of the films

Fig. 2 shows the XRD patterns of the films. Obviously, all the phase structures of the films are amorphous. It can be attributed to the high phase transition temperature of

Ta_2O_5 that is more than 873 K [13]. Previous studies showed that the high temperature of phase transition probably resulted from the remarkable complexity of Ta_2O_5 polymorphism [14].
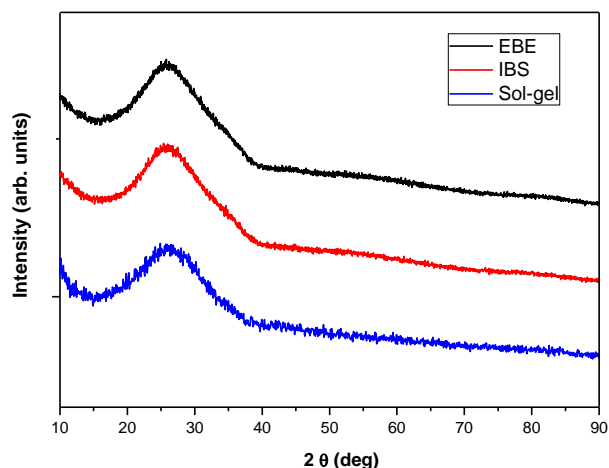
Fig. 2. XRD patterns of the films.

The AFM images recorded from the films are shown in Fig. 3. It illustrates that the preparation method has significant effects on the surface topographies of the films. The RMS roughness (σ) of the film is 1.01, 0.53 and 1.35 nm for the EBE, IBS and sol-gel films, respectively.

Fig. 4 shows the Ta 4f and O1s XPS spectra from the films. The Ta 4f spectra in Fig. 4(a) show $4f_{7/2}$ and $4f_{5/2}$ peaks, locating at 26.2 eV and 28.1 eV, respectively. Fig. 4(b) illustrates two peaks fitted from O 1s spectra, which points to two different chemical environments. All the films share the peak at 530.6 eV, which is related to Ta-O bonds. The other fitted peaks are 531.4, 531.1 and 532.6 eV for the EBE, IBS and sol-gel films, caused by contamination or organic components in the films. For each films, the binding energy difference $\Delta BE = BE(O\ 1s)-BE(Ta\ 4f_{7/2})$ is 504.4 eV, which confirms that the valence state of tantalum is Ta^{5+} [15-16]. The O/Ta ratio is estimated from the XPS peak areas with their relative sensitivity factors that are 0.66 for O 1s and 2.40 for Ta 4f. The O/Ta ratio is 2.5 for all the three films, indicating the stoichiometry.
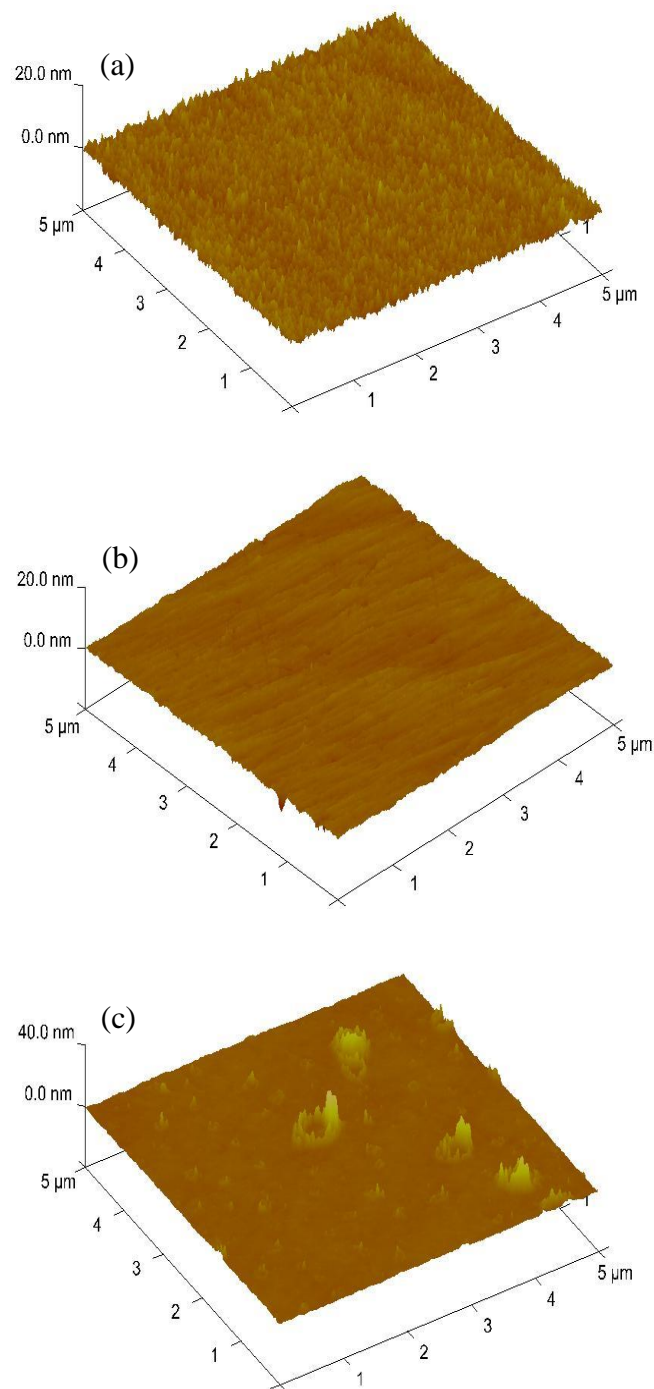
Fig. 3. AFM images of the films (a) EBE, (b) IBS and (c) Sol-gel.
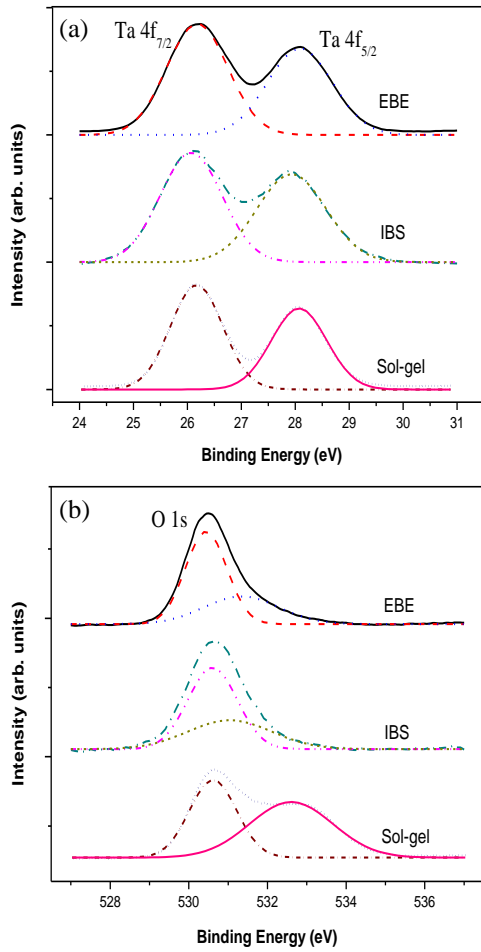
Fig. 4. XPS spectra of Ta 4f (a) and O1s (b) from the films.

film obtains the largest absorption, and then is the IBS film and the last is sol-gel film. The average absorption of the EBE, IBS and sol-gel films is 99.4, 55.8 and 20.1 ppm, respectively.

The impurity contents in the films detected by GDMS are shown in Table 1. It shows that the EBE film has the highest contents of impurities, whereas the impurity contents in the sol-gel film are the lowest. This is related to the starting material, coating equipment and deposition temperature. It is worthy to be noticed that high deposition temperature increases the volatilization of the residues absorbed on the coating equipment, resulting in more impurities in the film.

Table 1 Impurity contents in the films.

Films/Impurity contents (ppm)	Ni	Fe	Mo	Ti	Nb	W
EBE	9.6	26.5	11.9	25.6	22.8	18.7
IBS	<1	1.8	2.9	<1	3.7	<1
Sol-gel	<1	<1	<1	<1	<1	<1

The laser damage probabilities of the films are shown in Fig. 6. The LIDT of the EBE, IBS and sol-gel films is 8.3, 14.4 and 19.6 J/cm^2, respectively. From Figs. 5 and 6, it indicates that the absorption of films is larger, the LIDT is lower. It is also observed from Fig. 6 that the values at 100% damage probability show direct proportion to the LIDT results. In some extent, the 100% damage energy can be considered as the intrinsic damage threshold of the film, which is also highly in connection with the film absorption.

Fig. 5. Absorption of the films.

Fig. 5 shows the absorption of the films. To display the situation of different areas of the films, 10 points on each film are tested. Since the fluctuation of absorption is very small, the absorption for each film is even. The EBE
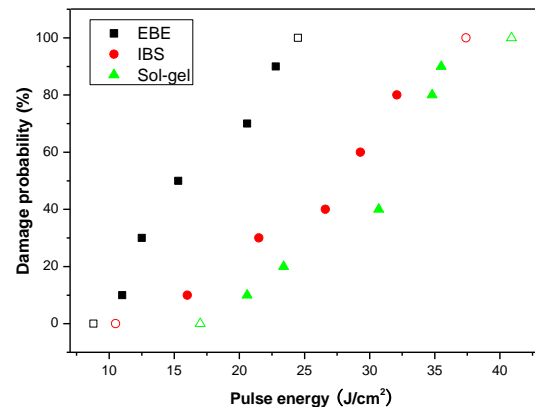
Fig. 6. Damage probabilities of the films.
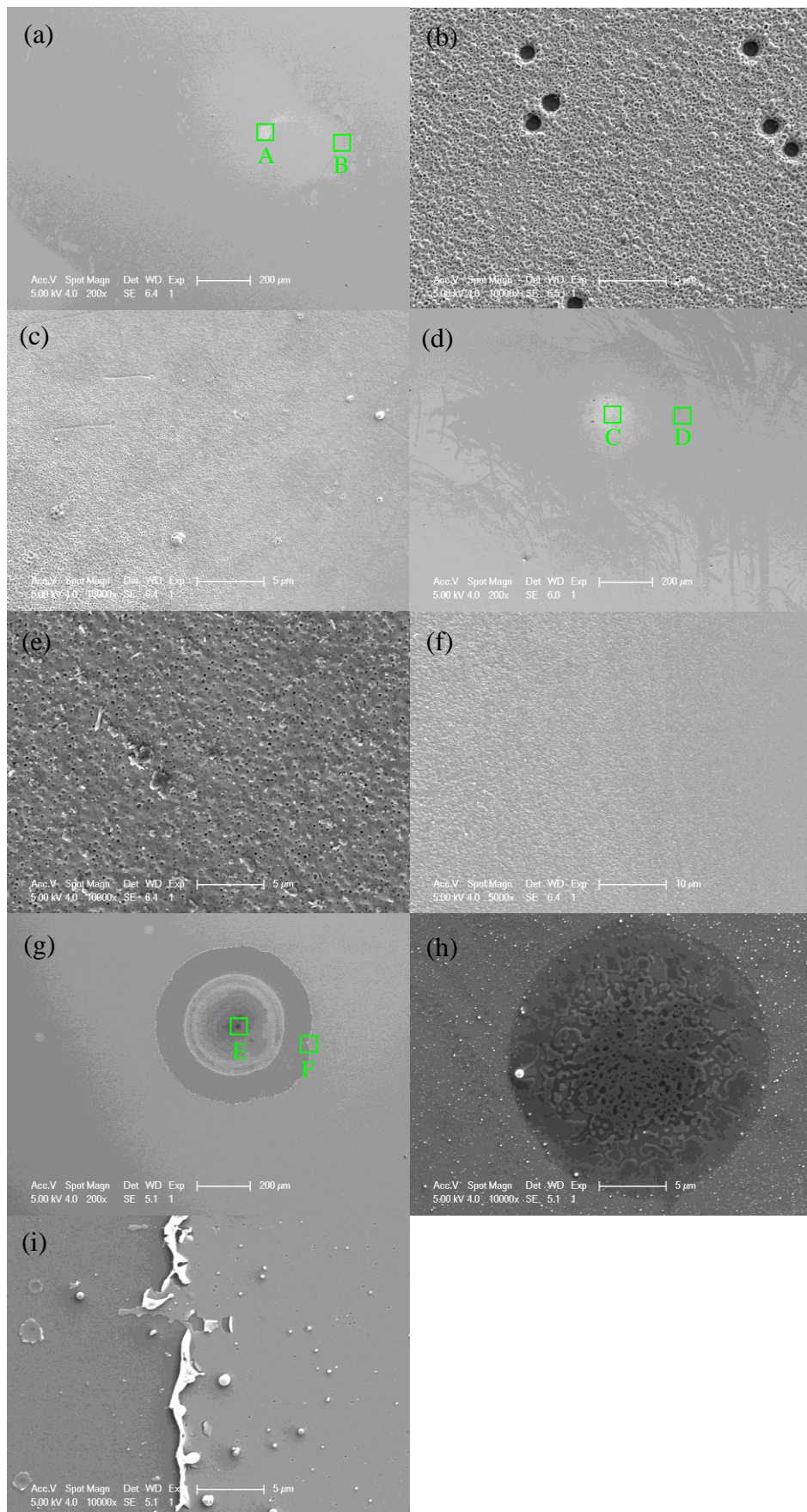
Fig. 7. Damage morphologies of the films (a) EBE, (b) enlarged A, (c) enlarged B, (d) IBS, (e) enlarged C, (f) enlarged D, (g) Sol-gel, (h) enlarged E and (i) enlarged F.

The damage morphologies of the films are shown in Fig. 7. Figs. 7(a), (d) and (g) show a general characteristic among the damage of these films, that is, a typical defect-induced damage with an apparent initiation center firstly appearing within the damage area and then spreading outward to turn into circular damage morphology. Fig. 7(b), the close-up image of A area of damage center in Fig. 7(a), illustrates some damage initiators in A area and many high-temperature-induced tiny pores in the damage area. Fig. 7(c) shows the enlarged morphology of B area at the damage border in which tiny pores in the damage center spread to the margin of the damage. Probably due to higher laser energy during the damage, less visible damage initiators compared with that in Fig. 7(b) and smaller pores in the damage area compared to those in the EBE film are shown in Fig. 7(e), the close-up image of C area of the damage center in Fig. 7(d). Besides, Fig. 7(f) shares the same morphology as the EBE film damage, the tiny pores spreading from the damage center to the margin of the damage. Both the EBE and IBS films present the thermal melt damage feature, as shown in Figs. 7(a)-(f). A large defect in E area, as shown in Fig. 7(h), makes the periodic damage rings in Fig. 7(g) after the high temperature melting under laser radiation. Different from Figs. 7(c) and (f), a flaking morphology is illustrated in Fig. 7(i), the close-up image of F area at the border of sol-gel film damage. As shown in Figs. 7(g)-(i), the sol-gel film indicates the damage feature of interaction between thermal melt and stress.

4. Discussion

It is well-known that the nanosecond laser-induced damage always arises as a result of strong absorption points which are induced by defects. Since the absorbance index of the defect is comparatively much higher than that of the film itself, more energy is absorbed by the defect under laser radiation, leading to the damage trigger point.

These defects can be divided into two types: the heterologous defects and the homologous defects. The heterologous defects have different elements from the film materials, which are also called impurities. The homologous defects only contain the elements originated from the film materials, which include substoichiometric defects and structural defects such as voids, nodules, grain boundaries and microcracks [17-18].

Consider a spherical impurity defect of radius a embedded in an infinite medium, where heat is produced in the sphere for the time $0 < t < t_p$ (t_p is the pulse length of the laser) at the constant rate A. The temperatures of the defect and the surrounding film satisfy the heating diffusion equation:

$$\begin{cases} \dfrac{1}{\kappa_d}\dfrac{\partial T_d}{\partial t} = \dfrac{1}{r^2}\dfrac{\partial}{\partial r}\left(r^2\dfrac{\partial T_d}{\partial t}\right) + \dfrac{A}{K_d}, 0 \le r < a, t > 0 \\[3mm] \dfrac{1}{\kappa_f}\dfrac{\partial T_f}{\partial t} = \dfrac{1}{r^2}\dfrac{\partial}{\partial r}\left(r^2\dfrac{\partial T_f}{\partial t}\right), r > a, t > 0 \end{cases}$$

(1)

when $0 < t < t_p$, $A = 3QI/4\pi a^3$ and when $t > t_p$, $A = 0$. The suffixes d and f refer to the defect and the surrounding film, respectively. T, K, κ, and I denote the temperature, thermal conductively, diffusivity and laser power intensity, respectively. Q is the absorption efficiency factor, and it can be calculated from the Mie scattering theory [19]. The boundary conditions are (a) at $t = 0$, $T_d = T_f = 0$; (b) when r = a, $T_d = T_f$ and $K_d(\partial T_d / \partial r) = K_f(\partial T_f / \partial r)$; and (c) T_d finite as $r \to 0$ and T_f finite as $r \to \infty$.

The final results for the temperatures of the defect and the surrounding film are given as [20]

$$\begin{cases} T_d = \dfrac{a^2 A}{K_d}\left\{\dfrac{1}{3}\dfrac{K_d}{K_f} + \dfrac{1}{6}(1 - \dfrac{r^2}{a^2}) - \right. \\[3mm] \left. \dfrac{2ab}{r\pi}\int_0^\infty e(\dfrac{-y^2 t_p}{\gamma})\dfrac{(\sin y - y\cos y)(\sin(ry/a)dy}{y^2\left[(c\sin y - y\cos y)^2 + b^2 y^2 \sin^2 y\right]}\right\}, 0 < r < a \\[3mm] T_f = \dfrac{a^3 A}{rK_d}\left\{\dfrac{1}{3}\dfrac{K_d}{K_f} - \dfrac{2}{\pi}\int_0^\infty e(\dfrac{-y^2 t_p}{\gamma}). \right. \\[3mm] \left. \dfrac{(\sin y - y\cos y)\left[by\sin y\cos\sigma y - (c\sin y - y\cos y)\sin\sigma y\right]dy}{y^2\left[(c\sin y - y\cos y)^2 + b^2 y^2 \sin^2 y\right]}\right\}, r > a \end{cases}$$

(2)

where $b = \left(K_f / K_d\right)\sqrt{\kappa_d / \kappa_f}$, $\gamma = a^2 / \kappa_d, c = 1 - K_f / K_d$ and $\sigma = \left(r / a - 1\right)\sqrt{\kappa_d / \kappa_f}$. In this study, FeO is considered as the impurity defect. The physical parameters of Ta_2O_5 and the defect are listed in Table 2 [21-22]. Supposing that the defect radii are 25 and 30 nm, respectively, the temperature rises of the defects radiated with the laser of 1064 nm and 12 ns are displayed in Fig. 8. For both the defects, the temperature increases with the increase of the laser energy. In addition, the damage of the 30 nm defect needs much less laser energy than that of the 25 nm defect, when reaching the same damage temperature such as the melting point of Ta_2O_5 (2153 K). If the film has higher impurity contents, it indicates that the impurity radius is larger or the density is higher. The former decreases the damage energy and the latter increases the damage probability. Both of these decrease the LIDT of the film. It is consistent with the LIDT results in Fig. 6. Therefore, the impurity content can be regarded as one of main influencing factors in the LIDT of the films.

Table 2 Thermal conductivity (K), density (ρ), specific heat (C), refractive index (n) and melting point (T) of the materials.

Materials	K (W/cm/K)	ρ (g/cm^3)	C (J/g/K)	n (at 1064 nm)	T (K)
Ta_2O_5	0.002	8.2	0.017	2.06	2153
FeO	0.00016	5.7	2.7	2.20	1643
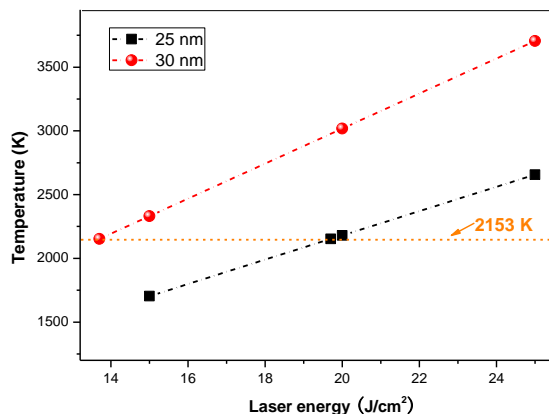
Fig. 8. Temperature rise of the defects under laser radiation.

The homologous defects also significantly affect the LIDT of the films. For example, substoichiometric defects such as the oxygen vacancies are very easy to generate in EBE films due to the high temperature deposition. Our previous results showed that oxygen vacancies were the most serious defects to decrease the LIDT of Ta_2O_5 films [5]. Thus annealing was adopted to eliminate the substoichiometric defects in the EBE film. As is shown in Fig. 4, all the three films are stoichiometric. Therefore, the effect of substoichiometric defects on the LIDT can be neglected here. Structural defects are another type of homologous defects, which also play an important role on the LIDT. It is reported that the nodule defects significantly decrease the LIDT and they are very difficult to be completely removed from EBE films especially. Since the EBE film has highest absorption and lowest LIDT, the structural defects may be another important influencing factor in the LIDT. By using the IBS method, due to the well-controlled stoichiometry and few structural defects, the deposited film always has lower absorption, thus obtaining higher LIDT than that of EBE film. Owing to the lowest deposition temperature that is always room temperature, the sol-gel film is well known as its stoichiometry and nearly free of structural defects, which are highly beneficial to the laser damage resistance.

Although the damage of all the films is initiated from defects, the different damage morphologies between the PVD and sol-gel films indicate that some other factors are also at work during the damage course. As is shown in Fig. 7, the PVD films present the thermal melt damage feature, whereas the sol-gel film shows the damage feature of interaction between thermal melt and stress. This difference is probably attributed to the acetylacetone in the sol-gel film. During the sol forming process, $TaCl_5$ first hydrolyzes to generate Ta_2O_5 nanoparticles. Then, these nanoparticles form clusters with the assistance of acetylacetone. At last, Ta_2O_5 clusters link together to construct an ordered three-dimensional network. The combination of Ta_2O_5 clusters and the low deposition temperature results in the large RMS roughness of the sol-gel film, which is confirmed by the AFM image in Fig. 3. Moreover, the special network structure leads to the low refractive index of the film, indicating the low packing density. Previous results showed that this low packing density was conducive to the formation of a more relaxed film structure which is more suitable for relieving the expansion of the skeleton when absorbing laser energy

[23-24]. Consequently, the least defects and the network structure contribute to the highest LIDT of the sol-gel film.

5. Conclusions

In summary, Ta_2O_5 films are prepared by EBE, IBS and sol-gel methods, respectively. The IBS film has the highest refractive index, and then is EBE film and the last is sol-gel film. The surface roughness of the IBS film is the smallest, while it is the largest for the sol-gel film. All the phase structures of the films are amorphous. The LIDT of the EBE, IBS and sol-gel films is 8.3, 14.4 and 19.6 J/cm^2, respectively. The least defects and the network structure contribute to the highest LIDT of the sol-gel film.

References

[1] H Yu, Y Shen, Y Cui, H Qi, J Shao, Z Fan, Appl. Surf. Sci. **254** 1783 (2008).

[2] G Tian, S Wu, L Yang, K Shu, L Qin, J Shao, Chin. Phys. Lett. **24,** 2967 (2007)

[3] Y Zhao, J Shao, H He, Z Fan Proc. SPIE **5991,** 599117-1 (2005).

[4] Y Zhao, Y Wang, H Gong, J Shao, Z Fan Appl. Surf. Sci. **210,** 353(2003).

[5] C Xu, P Yi, H Fan, J Qi, Y Qiang, J Liu, C Tao, D Li, Appl. Surf. Sci. **289,** 141 (2014).

[6] J Huang, G Tian, J Shao, Z Fan, Chin. Opt. Lett. **3,** 676 (2005).

[7] C Xu, D Li, H Fan, J Deng, J Qi, P Yi, Y Qiang Thin Solid Films **580,** 12 (2015).

[8] C Xu, P Yi, H Fan, J Qi, S Yang, Y Qiang, J Liu, D Li, Appl. Surf. Sci. **309,** 194 (2014).

[9] C Xu, D Li, H Fan, J Qi, J Deng, S Yang, P Yi, Y Qiang, Appl. Surf. Sci. **344,** 137 (2015).

[10] H He, X Li, S Fan, J Shao, Y Zhao, Z Fan, Proc. SPIE **5991,** 59912F (2005).

[11] H Hu, Z Fan, F Luo, Appl. Opt. **40,** 1950 (2001).

[12] ISO 11254-1:2000: lasers and laser-related equipment-determination of laser-induced damage threshold of optical surfaces. Part 1. 1-on-1 test

[13] J -P Masse, H Szymanowski, O Zabeida, A Amassian, J E Klemberg-Sapieha, L Martinu Thin Solid Films **515,** 1674 (2006).

[14] K Lehovec, J. Less-Common Met. **7,** 397 (1964).

[15] V A Shvets, V Sh Aliev, D V Gritsenko, S S Shaimeev, E V Fedosenko, S V Rykhlitski, V V Atuchin, V A Gritsenko, V M Tapilin, H Wong, J. Non-Cryst. Solids **354,** 3025 (2008).

[16] V V Atuchin, J -C Grivel, Z Zhang, Chem. Phys. **360,** 74 (2009)

[17] Y Zhao, W Gao, J Shao, Z Fan, Appl. Surf. Sci. **227,** 275 (2004)

[18] C Xu, J Ma, Y Jin, H He, J Shao, Z Fan, Chin. Phys. Lett. **25,** 1321(2008).

[19] P W Barber, S C Hill Light scattering by particles: computational methods (World Scientific) 1998

[20] H Goldenberg, C J Tranter, Br. J. Appl. Phys. **3,** 296 (1952).

[21] Z L Wu, M Reichling, X -Q Hu, K Balasubramanian, K H Guenther Appl. Opt. **32,** 5660 (1993).

[22] R L Orr, J. Am. Chem. Soc. **75,** 2808 (1953).

[23] F Chi, L Yan, H Lv, C Wang, X Yuan, Thin Solid Films **519,** 2483 (2011).

[24] X Li, M Gross, B Oreb, J J. Shen, Phys. Chem. C **116,** 18367 (2012)

_____

*Corresponding author: xucheng@cumt.edu.cn.